\$50 CH ELSEVIER

Contents lists available at ScienceDirect

## **Optics Communications**

journal homepage: www.elsevier.com/locate/optcom



# Design of efficient concave diffraction grating on 220 nm SOI platform for hybrid WDM–PDM (de)multiplexing



Ke Li, Jingping Zhu\*, Yuzheng Mao, Ning Zhang, Xun Hou

Key Laboratory for Physical Electronics and Devices of the Ministry of Education and Shaanxi Key Lab of Information Photonic Technique, School of Electronic Science and Engineering, Xi'an Jiaotong University, Xi'an 710049, China

## ARTICLE INFO

Keywords:
Concave diffraction grating (CDG)
Multiplexing
Polarization
Bragg reflector
Photonic band gaps

## ABSTRACT

An efficient concave diffraction grating (CDG) for multi-wavelengths and dual polarizations is proposed and demonstrated on 220 nm SOI platform with systematic analyzation and simulation. The multilayer dielectric reflector is designed as an alternative to conventional deep-etched tooth to provide high reflectance with polarization insensitivity. Simulation results indicate that with proper selection of incident angles, the grating designed by this approach shows excellent performances in terms of diffraction efficiency, channel uniformity and next-channel crosstalk for both TE and TM polarizations. A comparative analysis between different grating tooth configurations and a detailed discussion about the fabrication tolerances are also presented. This design can be applied to wavelength and polarization hybrid multiplexing to further enhance the link capacity of optical transmissions and interconnects.

#### 1. Introduction

With the rapid development of internet and cloud computing, the demand for data in optical communication and transmission is growing exponentially [1]. To further improve information capacity economically, advanced multiplexing technologies have attracted intensive attention in the past decades [2], which include wavelengthdivision-multiplexing (WDM) [3-5], polarization-division-multiplexing (PDM) [6], mode-division-multiplexing (MDM) [7-9]. Particularly, WDM has been widely used in the telecommunication schemes to enable transmissions of considerable channels in parallel by utilizing broad bandwidth available in the fiber infrastructure. Among the many technologies available in the WDM devices, concave diffraction grating (CDG) [10,11], a typical planar integrated circuit, is promising due to its significant advantages of compactness, relaxed fabrication tolerances and reduced costs. It contains only one laterally free propagation region (FPR), where the light originates from and is redirected into. Furthermore, the introduction of Bragg mirrors (consisting of alternating dielectric layers), as substitutes for deep-etched grating teeth, reduces the critical requirements on the verticality of grating facets [12]. The Bragg reflectors can provide a high reflectivity approaching 100% over a broad bandwidth and a wide angular range for a specific polarized light without complex metal coating process, as we have shown [13,14].

Nowadays, CDGs have been realized on various material platforms, such as silica-on-silicon [15], InP [16], polymer [4], and silicon-oninsulator (SOI) [17]. Among them, SOI enables ultra-compact integrated photonic devices due to its high index contrast and provides an attractive compatibility with mature CMOS processes. It is worth noting that the difference in effective indices of the slab waveguide of transverse electric (TE) and transverse magnetic (TM) polarizations results in a different power efficiency for a given diffracted order and a significant shift in the spectral response [18]. Therefore, many diffraction gratings are designed for only one polarization [5,14]. However, in optical communication system, the optical signal generally has indeterminate polarization state, which means a significant portion of light transmitting through the polarization dependent CDG is diffracted away from desired receiving waveguides [19]. To eliminate the disparity of effective indices, D. Feng et al. propose a 12 channel echelle grating demultiplexer, utilizing a thicker core layer (e.g. a 3-µm SOI platform), which has an 8-nm channel spacing, 1.7-dB on-chip loss with polarization insensitivity [20]. In such structure, the effective indices of TE and TM polarizations of the same order converge, but a 200 nm layer of high reflectivity aluminum needs to be deposited on the grating facets. Furthermore, there is a deterioration of performance caused by excitation of higher order modes due to the nonvertical grating facets. The output waveguides have to be located very close to the grating normal to avoid high crosstalk and losses, therefore resulting in a large footprint.

E-mail address: jpzhu@xjtu.edu.cn (J. Zhu).

Corresponding author.

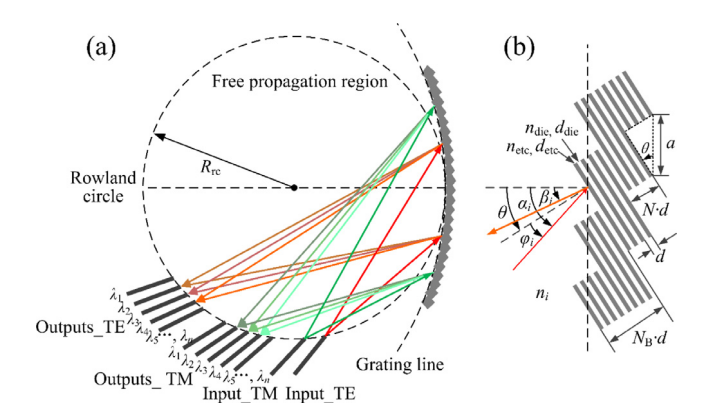


Fig. 1. Schematic layout of (a) the Bragg-CDG based on Rowland configuration and (b) the flat diffraction grating based on Bragg mirrors.

Wavelength and polarization hybrid multiplexing, which enable WDM and PDM simultaneously, is an alternative way to utilize input signals of dual polarizations. In this way, the link capacity can be doubled without extra lasers compared with previous wavelength (de)multiplexer. In this paper, we present for the first time a dual-input (i.e., TE and TM polarized light, respectively) Bragg-CDG on a 220 nm SOI platform, which is available for PDM-WDM systems. The incoming light is divided into two polarized beams by the polarization-beam splitters (PBSs) [21], which are incident into the CDG with different angles and then refocused on different positions after efficient diffraction of the grating. A 16-channel (8 wavelengths and dual polarizations) CDG is realized along with reasonable crosstalk and insertion losses. as an example. This paper is organized as follows. Section 2 shows design concepts and optical conditions of the grating. The design of a polarization-independent Bragg reflector, numerical spectral response and comparison of the grating with different tooth configurations are demonstrated in Section 3.1, Section 3.2, and Section 3.3, respectively. The impact of various imperfections in fabrication process is also discussed in Section 4. Finally, some conclusions are summarized in Section 5.

## 2. Principle and design method

The schematic layout of the Bragg-CDG based on Rowland mounting for hybrid WDM–PDM multiplexing is illustrated in Fig. 1(a). Input waveguides (InWGs) and output waveguides (OutWGs) are placed on the Rowland circle (RC) with radius of  $R_{\rm rc}$ . The grating is composed of a series of continuous Bragg reflectors (i.e., alternating strips), which are curved along a circular grating line with radius equal to the diameter of the RC. The grating circle is tangent to the RC at the grating pole. With Bragg reflection condition matched with grating diffraction condition for both TE and TM polarizations, the dual-input light in Fig. 1(a) can be diffracted and refocused into respective outputs according to polarizations and wavelengths.

It is convenient to analyze the reflection and diffraction characteristics of this concave grating by corresponding flat grating, as shown in Fig. 1(b). The effective index of FPR is  $n_i$  (i=1 represents TE polarization and i=2 represents TM here). The widths of a dielectric layer and an etched layer are  $d_{\rm die}$  and  $d_{\rm etc}$  with indices of  $n_{\rm die}$  and  $n_{\rm etc}$ , respectively, creating a Bragg period  $d=d_{\rm die}+d_{\rm etc}$ . The filling fraction is defined as  $f=d_{\rm die}/d$ .  $N_{\rm B}$  and N are the number of Bragg periods per Bragg reflector and per diffraction grating period a, respectively. The angles displayed in Fig. 1(b) are given as follows: blazing angle or tilt angle of the grating  $\theta$ ; incident angle relative to the facet normal  $\varphi_i$ ; incident and diffraction angles with related to the grating normal  $a_i$  and  $\beta_i$ .

As an example, a 220-nm-thick SOI wafer is considered to be monomode and double-polarization for the slab waveguide. A series

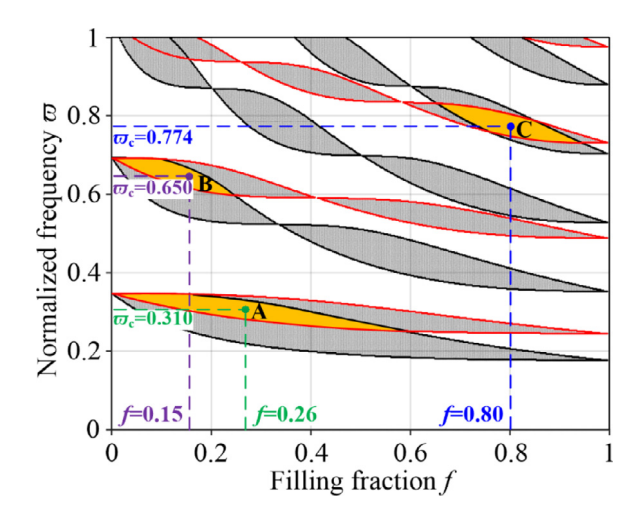


**Fig. 2.** Band structure of the Bragg reflector on the  $\varpi$ -f plane with  $\varphi_1=\varphi_2=2^\circ$ ,  $N_{\rm B}=14$  and refraction indices  $n_1=2.848$  (TE),  $n_2=2.053$  (TM) and  $n_{\rm etc}=1.444$ . The black and red lines represent the band edges of TE and TM modes, respectively. Propagating state, white; band gap, gray; band gap overlap, orange.. (For interpretation of the references to color in this figure legend, the reader is referred to the web version of this article.)

of trenches are fully etched to the buried oxide layer and replaced by  ${\rm SiO_2}$  ( $n_{\rm die}=n_i,\ n_{\rm etc}=1.444$ ). In this case, the effective indices for TE and TM fundamental modes at the central wavelength  $\lambda_c=1.55~\mu{\rm m}$  are  $n_1=2.848$  and  $n_2=2.053$ , respectively. The propagation characteristics of a Bragg reflector can be calculated by one dimensional photonic crystal (1D PC) bandgap theory. As shown in Fig. 2, the photonic band gaps of such a periodic structure (alternation of Si and  ${\rm SiO_2}$ ) with  $\varphi_1=\varphi_2=2^\circ$  and  $N_{\rm B}=14$  is calculated and drawn on  $\varpi$ -f plane. The ordinate  $\varpi$  indicates the normalized frequency, which is defined as

$$\varpi = \frac{d\omega}{2\pi c} = \frac{d}{\lambda},\tag{1}$$

with c,  $\lambda$  and  $\omega$  the light speed in vacuum, operation wavelength and angular frequency, respectively.

The black and red solid lines represent the band edges of TE and TM fundamental modes, respectively, where Block wave number K is equal to zero. The white spaces are regions of propagating states (K is strictly real), whereas the gray areas represent regions existing photonic band gaps (K is imaginary). The orange areas are the overlap among band gaps of the two polarization states, where dual polarized light can be reflected efficiently within a certain frequency range.

On the other hand, to achieve optimum diffraction, grating equation have to be fulfilled [11],

$$m_i \lambda = n_i a \left( \sin \alpha_i + \sin \beta_i \right) \quad i = 1, 2,$$
 (2)

with  $m_i$  the diffraction order. The diffraction grating and the Bragg reflector work constructively together when the incident and diffraction light is mirror-symmetrical about the facet normal,

$$\beta_i - \theta = -\varphi_i \quad i = 1, 2, \tag{3}$$

i.e., the blazing condition. Furthermore, from the grating geometry in Fig. 1(b), we have

$$a = Nd / \sin \theta. \tag{4}$$

With the use of Eqs. (1), (3) and (4), Eq. (2) is then transformed into

$$m_i = 2n_i N \varpi \cos \varphi_i \quad i = 1, 2. \tag{5}$$

Considering Eq. (5) and the band structure in Fig. 2, the central normalized frequency  $\varpi_c$ , corresponding to  $\lambda_c$ , can be obtained with proper  $m_i$  and N selected. Then d is derived from Eq. (1). The filling

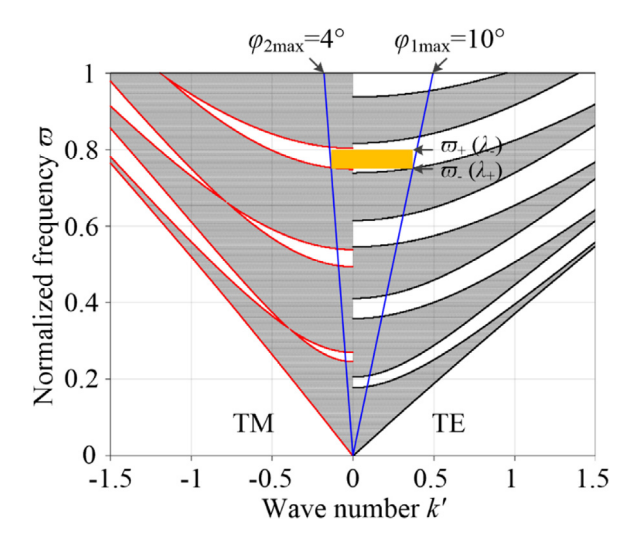


**Fig. 3.** Band structure of the Bragg reflector on the  $\varpi$ -k' plane with f=0.8,  $N_{\rm B}=14$  and refraction indices  $n_1=2.848$  (TE),  $n_2=2.053$  (TM) and  $n_{\rm etc}=1.444$ . The black and red lines represent the band edges of TE and TM, respectively. Propagating state, white; band gap, gray; band gap overlap, orange.. (For interpretation of the references to color in this figure legend, the reader is referred to the web version of this article.)

fraction f is determined to ensure adequate reflection bandwidth for both polarizations.

In addition, it is worth noting that in previous band gap model, the incident angles of dual polarizations are set to be equal ( $\varphi_1 = \varphi_2=2^\circ$ ). However, in practice, it is values of the two incident angles

that determine the spatial layout of access waveguides and even limit diffraction efficiencies. Here, three conditions need to be fulfilled.

Firstly, the desired waveband from  $\lambda_-$  to  $\lambda_+$  should fall within the band-gap overlaps of the two polarizations. Fig. 3 shows the band structure with f=0.8 on  $\varpi$ -k' plane (propagating state, white; band gap, gray), in which the positive and negative semi-axes represent TE-mode and TM-mode, respectively.  $k'=\frac{dk_y}{2\pi}=\frac{dn_l\sin\varphi_l}{\lambda},\ i=1,2$  with  $k_y$  the wave vector component in dielectric layer perpendicular to the facet normal, and then  $\varpi=\frac{k'}{n_l\sin\varphi_l},\ i=1,2$  [14]. It means that the slope of a diagonal line is inversely proportional to the sine of incident angle. For a given Bragg period d, the normalized frequency range from  $\varpi_-=d/\lambda_+$  to  $\varpi_+=d/\lambda_-$  can be obtained, as shown in the orange area in Fig. 3. The lower boundary of this zone intersects with band edges of TE (black line) and TM (red line) modes at one point, respectively, corresponding to incident angles of  $\varphi_{1\max}$  ( $\varpi=\frac{k'}{n_1\sin\varphi_{1\max}}$ ) and  $\varphi_{2\max}$  ( $\varpi=\frac{k'}{n_2\sin\varphi_{2\max}}$ ). Then, the desired band can be efficiently reflected with  $\varphi_1 \leq \varphi_{1\max}$  and  $\varphi_2 \leq \varphi_{2\max}$ .

Next, the two output arrays should be separated completely, i.e.,

$$\beta|_{\text{TM}, \lambda = \lambda_1} - \beta|_{\text{TE}, \lambda = \lambda_j} \ge \frac{d\beta}{d\lambda}|_{\text{TE}, \lambda = \lambda_j} \cdot \Delta\lambda,$$
 (6)

where  $\Delta\lambda$  and j are the adjacent channel spacing and the number of wavelength channels of each polarization, respectively.  $\beta|_{\mathrm{TM},\,\lambda=\lambda_1}$  and  $\beta|_{\mathrm{TE},\,\lambda=\lambda_j}$  are the diffraction angle of TM-mode in the minimum channel wavelength  $\lambda_1$  and that of TE-mode in the maximum channel wavelength  $\lambda_j$ , respectively.  $\frac{\mathrm{d}\beta}{\mathrm{d}\lambda}|_{\mathrm{TE},\,\lambda=\lambda_j}$  is the angular dispersion of TE in  $\lambda_j$ , obtained by differentiating the grating equation,

$$\frac{\mathrm{d}\beta}{\mathrm{d}\lambda}|_{\mathrm{TE},\,\lambda=\lambda_{j}} = \frac{m_{1}}{n_{1}Na\cos\beta|_{\mathrm{TE},\lambda=\lambda_{j}}}.$$
 (7)

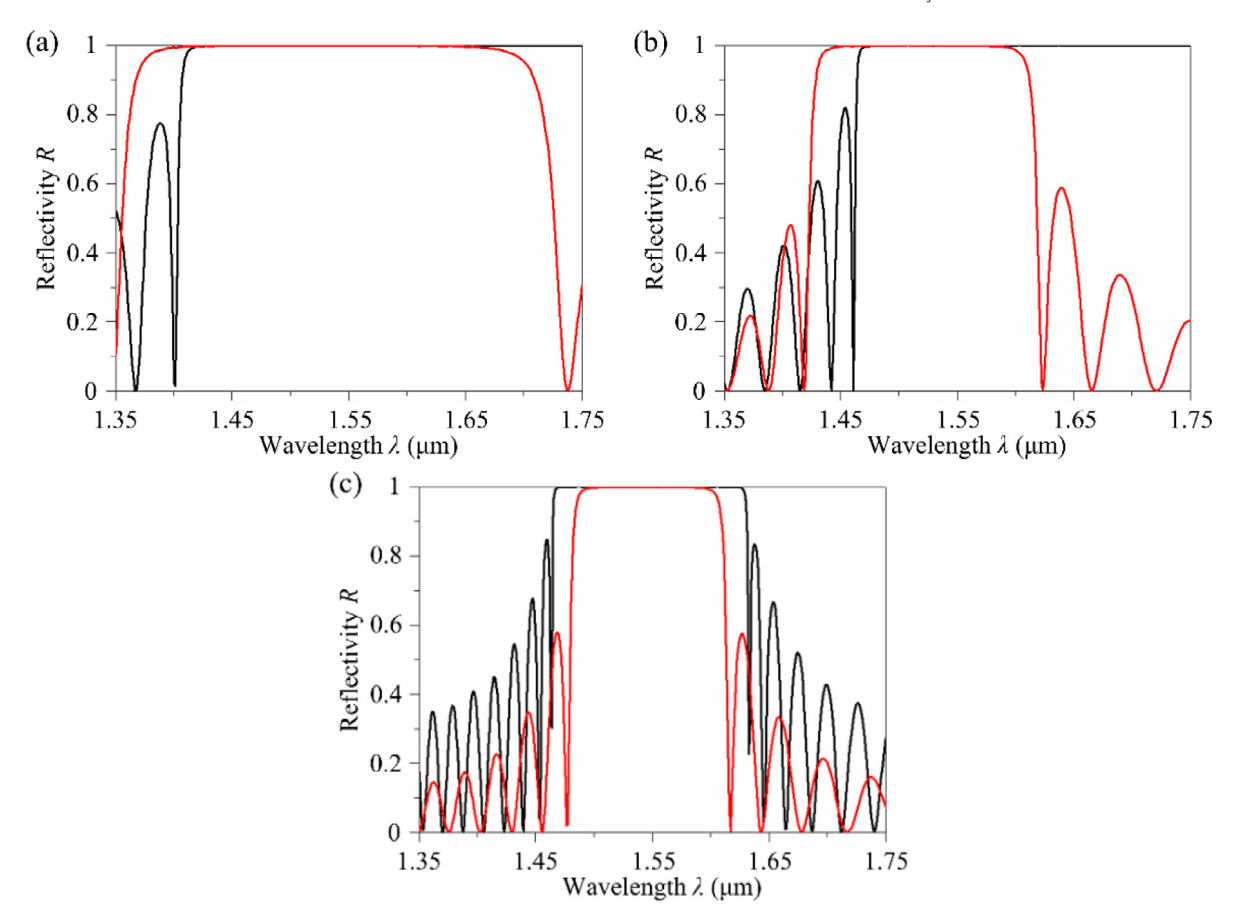


Fig. 4. Reflection spectra for TE (black line) and TM (red line) modes of (a) grating A; (b) grating B; (c) grating C.

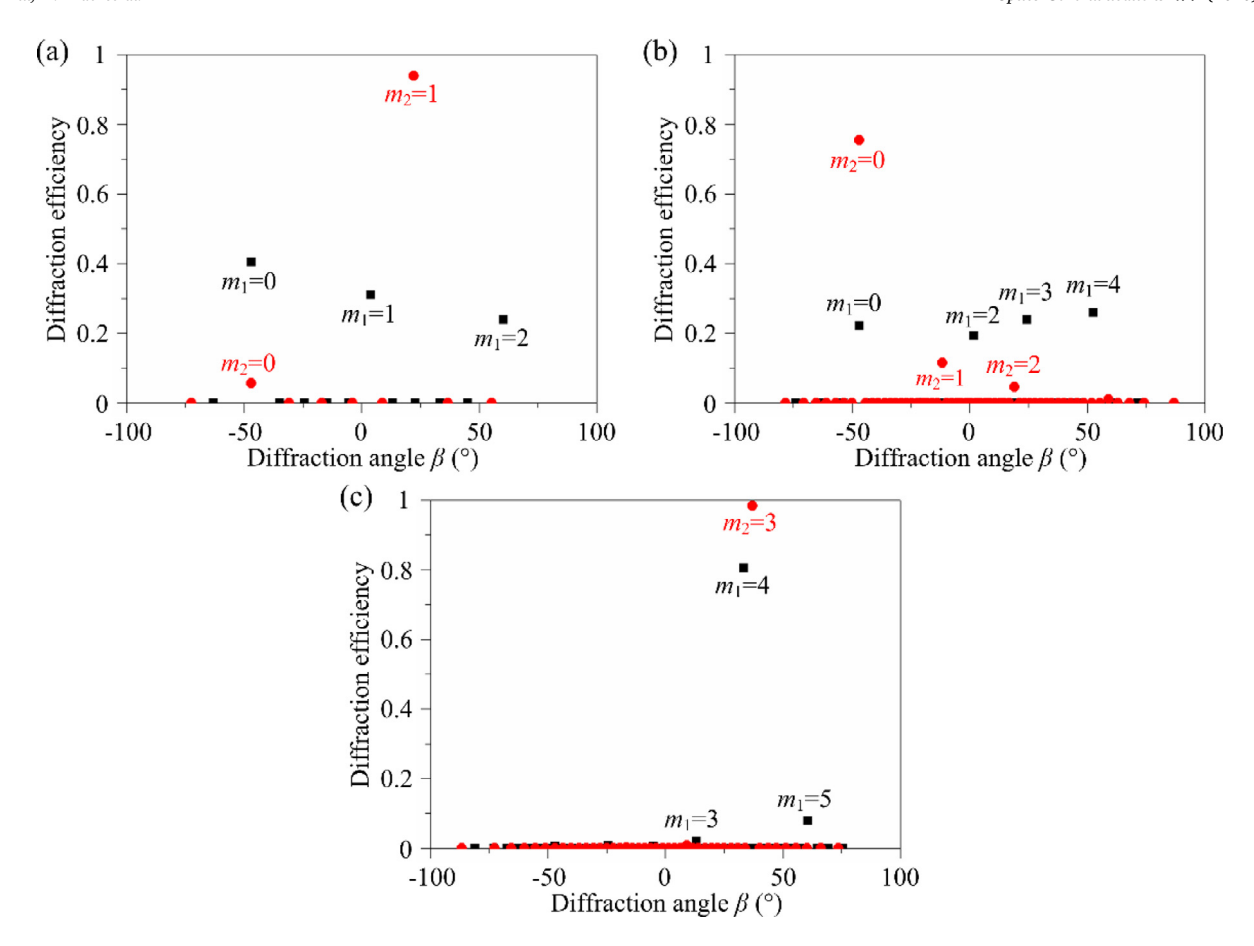


Fig. 5. Diffraction efficiency distributions in all directions at the central wavelength for TE (black square) and TM (red circle) modes of (a) grating A, (b) grating B and (c) grating C. The poor blazing of gratings A and B leads to a lower diffraction efficiency of the main order.

Separation of InWGs and OutWGs is considered finally, which can be expressed as

$$\theta + \varphi_2 - \beta|_{\text{TM}, \, \lambda = \lambda_j} \ge \frac{\mathrm{d}\beta}{\mathrm{d}\lambda}|_{\text{TE}, \, \lambda = \lambda_j} \cdot \Delta\lambda,\tag{8}$$

with  $\beta|_{\mathrm{TM},\lambda=\lambda_j}$  the diffraction angle of TM-mode in  $\lambda_j$ . Using the above design method, an efficient CDG configuration for dual polarizations can be implemented.

## 3. Numerical simulation and analysis

With this method, a CDG is designed and optimized on the SOI platform The substrate is an SOI wafer with a 220 nm silicon layer on top of a buried oxide layer, which is then covered by a 3  $\mu m$  silica cladding layer. The access waveguides and alternating strips are defined by the fully deep-etch of the silicon. All the following designs and optimizations are performed at room temperature.

#### 3.1. Designing of polarization-independent reflector

As shown in Fig. 2, the green, purple and blue dashed lines indicate three Bragg reflectors with varied central normalized frequency  $\varpi_c$  and filling fraction f in the band-gap overlaps. Then, the Bragg period d is deduced by  $d=\varpi_c\times\lambda_c$ . With N=1 and  $\theta=45^\circ$ , a is derived from Eq. (4), as listed in Table 1. Using the effective indices  $n_1$  and  $n_2$  previously mentioned, reflection spectra of these reflectors for TE (black line) and TM (red line) polarizations are simulated by the finite-difference time-domain (FDTD) method in a two-dimensional way and presented in Fig. 4.

Note that for the two polarization states, grating A [Fig. 4(a)] has a high reflectivity of almost 100% over a broad bandwidth of about

Table 1
Design parameters of the gratings.

Parameter	A	В	С
Central normalized frequency $\varpi_c$	0.310	0.650	0.774
Filling fraction f	0.26	0.15	0.80
Bragg period $d$ ( $\mu$ m)	0.481	1.008	1.200
Grating period a (μm)	0.680	1.426	1.710

260 nm around the central wavelength. Furthermore, for grating B [Fig. 4(b)] and grating C [Fig. 4(c)], similar reflection efficiencies are obtained with reflection bandwidths of about 150 nm and 100 nm, reflectively. Therefore in all three cases, the Bragg mirror could provide a very large reflection bandwidth for dual polarizations.

To briefly describe the diffraction characteristics of these three gratings, the far-field power distributions of different diffraction angles of the corresponding flat gratings are simulated at the central wavelength, as shown in Fig. 5. Black squares and red circles represent TE (with diffraction orders of  $m_1$ ) and TM (with diffraction orders of  $m_2$ ) polarizations, respectively. As indicated in Fig. 5(a), almost all the power of TM mode gets diffracted into the first-order in grating A; while for TE mode, varied orders coexist and more than 40% of the power is diffracted into zero-order without dispersion. Then, in Fig. 5(b) (grating B), a large portion of lights (about 75%) of TM mode is diffracted into zero-order, and the power of TE mode is distributed over four orders almost evenly. In contrast, for grating C [Fig. 5(c)], the major power is diffracted into a single non-zero order for both TE mode  $(m_1 = 4)$ and TM mode ( $m_2 = 3$ ), and high grating efficiencies of up to 81% and 98% can be obtained, respectively. Therefore, grating C which is more aligned with Eq. (5) compared with gratings A and B, is a

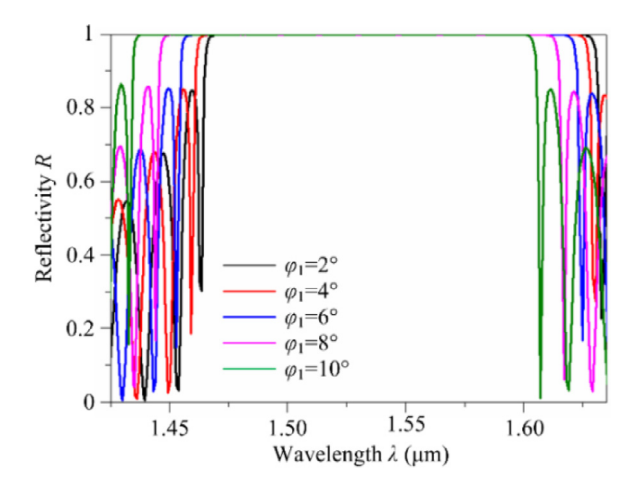


Fig. 6. Reflection spectra of grating C for TE polarized light incident at different angles.

relatively ideal configuration for wavelength and polarization hybrid multiplexing with efficient diffractions for both polarizations.

As for the two incidents angles, three conditions for grating C are calculated as follows. Firstly, in Fig. 3, the upper and lower boundaries of the orange area represent  $\varpi_{+} = 0.8$  and  $\varpi_{-} = 0.75$ , respectively. The grating is designed for 10 channels (5 wavelengths and dual polarizations) centered around the wavelength of  $\lambda_c = 1.55 \ \mu m$  with an inter-channel spacing of  $\Delta \lambda = 16$  nm. Thus, the minimum and maximum channel wavelengths are selected as  $\lambda_1 = 1.518 \mu m$  and  $\lambda_5 = 1.582 \mu m$ , respectively. The corresponding reflection waveband for grating C ranges from  $\lambda_{-} = 1.5 \, \mu \text{m}$  to  $\lambda_{+} = 1.6 \, \mu \text{m}$ , which is large enough for the operating wavelength range. The intersections between the lower boundary of this zone and the band edges of TE and TM polarizations indicate the incident angles of  $\varphi_{1\text{max}}$ =10° and  $\varphi_{2\text{max}}$ =4°, respectively. Therefore, when  $\varphi_1 \le 10^\circ$  and  $\varphi_2 \le 4^\circ$ , sufficient reflection bandwidth can be obtained. Take TE mode as an example, the reflection spectra with varied incident angles from 2° to 10° are simulated and demonstrated in Fig. 6. It can be seen that as  $\varphi_1$  increases, there is an obvious blue-shift, but the spectrum from 1.5 to 1.6 µm always retains high reflectivity, which is consistent with the theoretical results.

Furthermore, in the other two conditions of  $\varphi_1$  and  $\varphi_2$ , i.e., Eqs. (6) and (8), the diffraction angles are determined by Eq. (2) and related to the incident angles. Therefore, in this case, Eqs. (6) and (8) can be transformed into

$$\arcsin \left[ 1.307 - \sin \left( 45^{\circ} + \varphi_{2} \right) \right] - \arcsin \left[ 1.309 - \sin \left( 45^{\circ} + \varphi_{1} \right) \right]$$

$$\geq \frac{0.013}{\sqrt{0.904 + \cos^{2} \left( 45^{\circ} + \varphi_{1} \right)}}, \tag{9}$$

$$45^{\circ} + \varphi_2 - \arcsin\left[1.362 - \sin\left(45^{\circ} + \varphi_2\right)\right] \ge \frac{0.013}{\sqrt{0.904 + \cos^2\left(45^{\circ} + \varphi_1\right)}}.$$
(10)

Then these three conditions of incident angles can be drawn in one figure, as shown in Fig. 7(a), and eventually, the incident angles have values as  $\varphi_1$ =6° and  $\varphi_2$ =2° [see point P in Fig. 7(a)].

## 3.2. Spectra response

The CDG is defined by a series of Bragg reflectors connected continuously along the grating circle. According to linear dispersion equation of the grating, the center to center spacing  $\Delta l_i$  between adjacent channels for each input is deduced as

$$\Delta I_i = \frac{2R_{\rm rc}m_i\Delta\lambda}{n_iNa} \quad i = 1, 2. \tag{11}$$

Thus, the ratio of  $\Delta l_1$  to  $\Delta l_2$  is dependent on  $m_i$  and  $n_i$  with the form as

$$\frac{\Delta l_1}{\Delta l_2} = \frac{m_1 n_2}{m_2 n_1}.\tag{12}$$

With  $m_1 = 4$  and  $m_2 = 3$ ,  $\Delta l_1 = 5$  µm is chosen for TE mode, leading to  $\Delta l_2 \approx 5.20$  µm from Eq. (12) and  $R_{\rm rc} = 188.8$  µm from Eq. (11).

A numerical simulation of the CDG is carried out and then spatial distributions of lights at wavelengths of 1.518  $\mu m$  and 1.582  $\mu m$  are displayed in Fig. 8, which illustrate the diffraction characteristics intuitively. Firstly, for TE mode, major power is diffracted into the order of  $m_1=4$  with a small amount distributed into other orders such as  $m_1=3$  and  $m_1=5$ . Then for TM mode, almost all power is collected in the desired diffraction order of  $m_2=3$ . Moreover, it is obvious that all access waveguides are completely separated, which permits a better crosstalk level.

To fully estimate the total on-chip loss, a 30 µm long linear taper is added to provide adiabatic propagation and connect the silicon nanowire and the access waveguide from 0.5 µm to 4.4 µm. The footprint of whole device is 0.5×0.5 mm<sup>2</sup>. The diffraction spectra (Fig. 9) of this configuration are simulated using 2.5D FDTD propagator (varFDTD) of Mode Solutions, with input wavelengths from 1.5 to  $1.6~\mu m$ . The results show a high efficiency of 86% (-0.65 dB) for TE polarization [Fig. 9(a)], with a channel uniformity of 0.47 dB, as well as a high efficiency of 93% (-0.32 dB) for TM [Fig. 9(b)], with a channel uniformity of 0.34 dB. The polarization-dependent loss over the available channels is less than 0.5 dB, which could be further reduced by differential design of OutWGs width of the two polarizations, either by further optimization of the grating. Additionally, the next-channel crosstalk for TM polarization is about -30 dB, better than -25 dB for TE. This is simply because the gap between OutWGs of TM polarization of  ${\sim}0.8~\mu m$  is slight wider than that of TE of  ${\sim}0.6~\mu m$ .

Moreover, when  $R_{\rm rc}$  increases to 302.1 µm, a channel spacing of 10 nm with 16 channels (8 wavelengths and dual polarizations) can also be achieved. The minimum and maximum channel wavelengths are  $\lambda_1=1.51~\mu{\rm m}$  and  $\lambda_8=1.58~\mu{\rm m}$ , respectively. The final footprint of the device is approximately 0.8×0.6 mm². As shown in Fig. 10, the diffraction grating efficiency is 74% (–1.30 dB) for TE polarization with channel uniformity of 0.58 dB and next-channel crosstalk better than –20 dB. For TM polarization, the grating efficiency is up to 85% (–0.70 dB) with channel uniformity of 0.35 dB and crosstalk of –23 dB. Table 2 shows the reported performances of different diffraction grating designs, made on the SOI platform. We can see that compared with other devices, our design can provide efficient diffraction for dual polarizations with a compact size, and reasonable crosstalk and insertion losses.

## 3.3. Comparison of different tooth configurations

The gratings designed above contain one Bragg period per diffraction grating period (N = 1). It is noticeable that as  $N \neq 1$ , there is some possibility to work with  $m_1$  and  $m_2$  solved from Eq. (5) both close to integers (therefore working at blazing condition). After calculation with varied N and the same  $\varpi_c$  and f as grating C, we find that when per diffraction grating period contains 5 Bragg periods (N = 5), the diffraction orders obtained by Eq. (5) for the two polarizations at the central wavelength are approximate to  $m_1 = 22$  and  $m_2 = 16$ , respectively. To perform a comparison with the situation of N=1,  $R_{\rm rc}$  has been reduced to 171.6  $\mu m$  this time to keep similarity of  $\Delta l_1$ with the previous case, and then  $\Delta l_2$  is about 5.04 µm from Eq. (12). In this case, Fig. 7(b) shows the three conditions of incident angles, and then  $\varphi_1=9^\circ$  and  $\varphi_2=3^\circ$  are selected [see point Q in Fig. 7(b)]. Fig. 11 shows the spatial distribution of lights at  $\lambda_c$ . It can be seen that for both polarizations, most of lights get redirected into the specified order, but more varied diffraction orders arise in comparison with Fig. 8.

Moreover, high diffraction order leads to a limited free spectral range. This means that a slight shift of wavelength would result in a

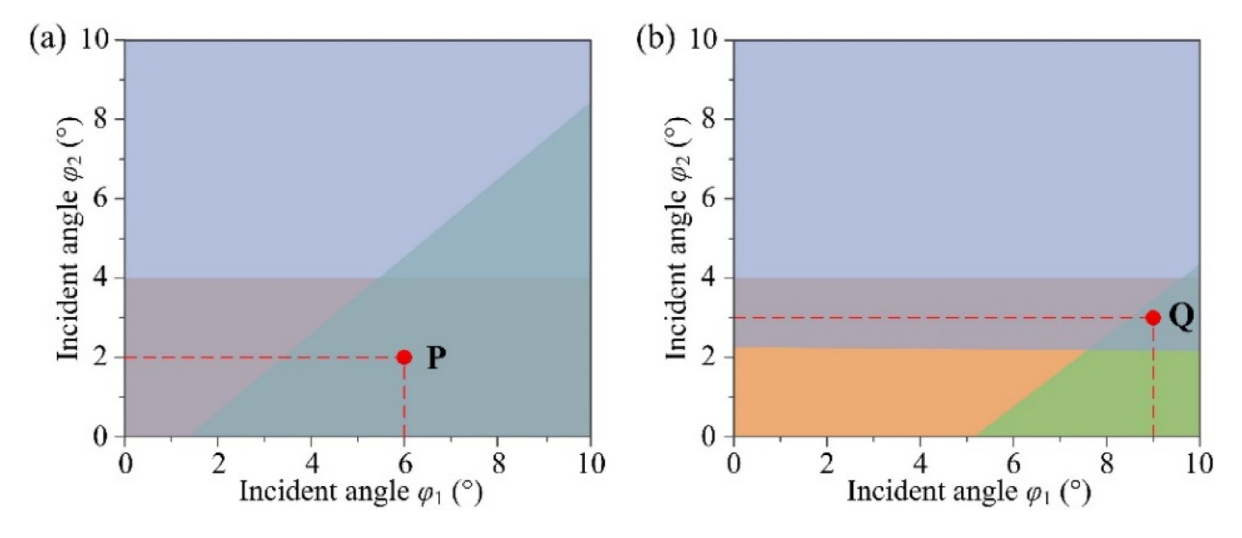


Fig. 7. Three conditions of the two incident angles with (a) N = 1 and (b) N = 5. Condition 1, orange; condition 2, green; condition 3, blue. (For interpretation of the references to color in this figure legend, the reader is referred to the web version of this article.)

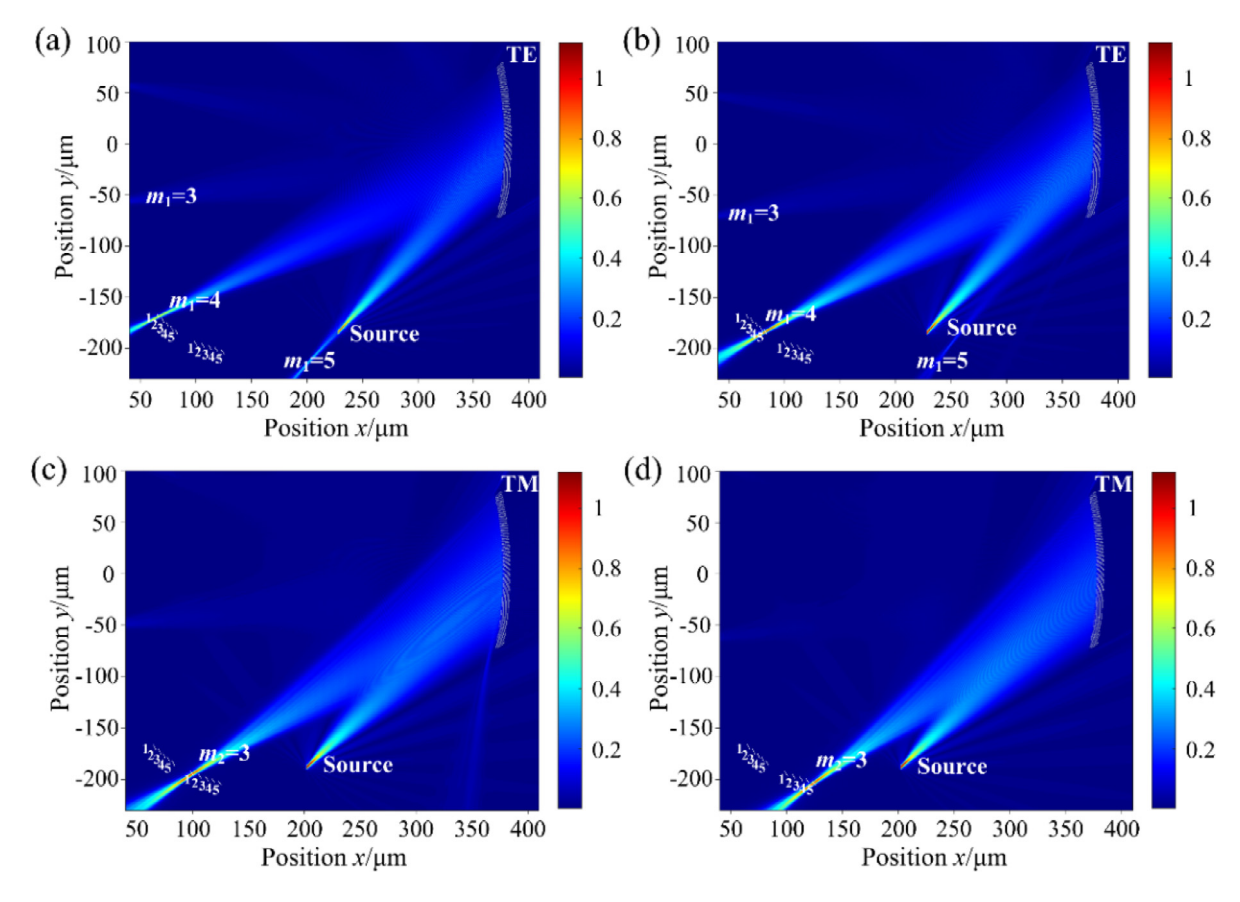


Fig. 8. Spatial distributions of lights in the CDG with one Bragg period per diffraction grating period (N=1) for (a) TE mode at 1.518  $\mu$ m; (b) TE mode at 1.582  $\mu$ m; (c) TM mode at 1.518  $\mu$ m; (d) TM mode at 1.582  $\mu$ m.

variation of the main diffraction order, which can be inferred from Eq. (5). The spatial distribution of TE polarized beam at wavelengths of 1.518  $\mu$ m and 1.582  $\mu$ m is demonstrated in Fig. 12. It can been seen that at wavelength of 1.518  $\mu$ m, most of lights are still diffracted into the order of  $m_1=22$  with a small portion into adjacent order of  $m_1=23$ ; while at higher wavelength, most power is diffracted into the order of  $m_1=21$ , leading to a significant decline of power in the designed order. Furthermore, there are obvious overlaps between the diffraction angles

at different wavelengths and diffraction orders, which deteriorate the device crosstalk level significantly.

Fig. 13 displays the diffraction spectra with the same width of access waveguides as the configuration of N=1. When the wavelength deviates from the central wavelength, the output channel (e.g. channel 1 in black line and channel 5 in green line) would collect not only lights of desired wavelength of the main diffraction order, but also a significant level of lights of other wavelengths from other diffraction orders. Compared with the case of N=1, the efficiencies here for

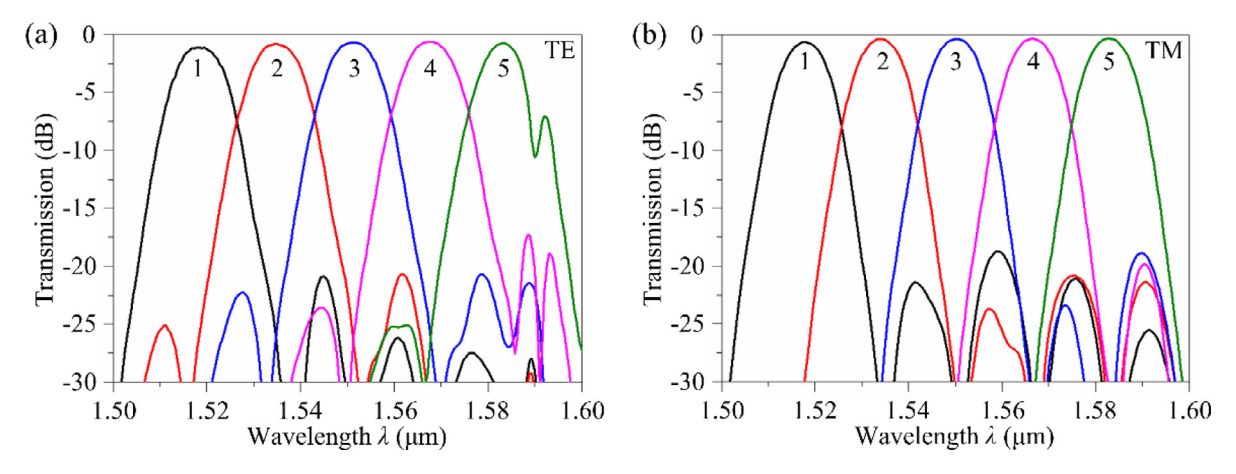


Fig. 9. Output spectra of the CDG with N=1 and  $\Delta\lambda=16$  nm for (a) TE  $(\varphi_1=6^\circ)$  and (b) TM  $(\varphi_2=2^\circ)$  modes.

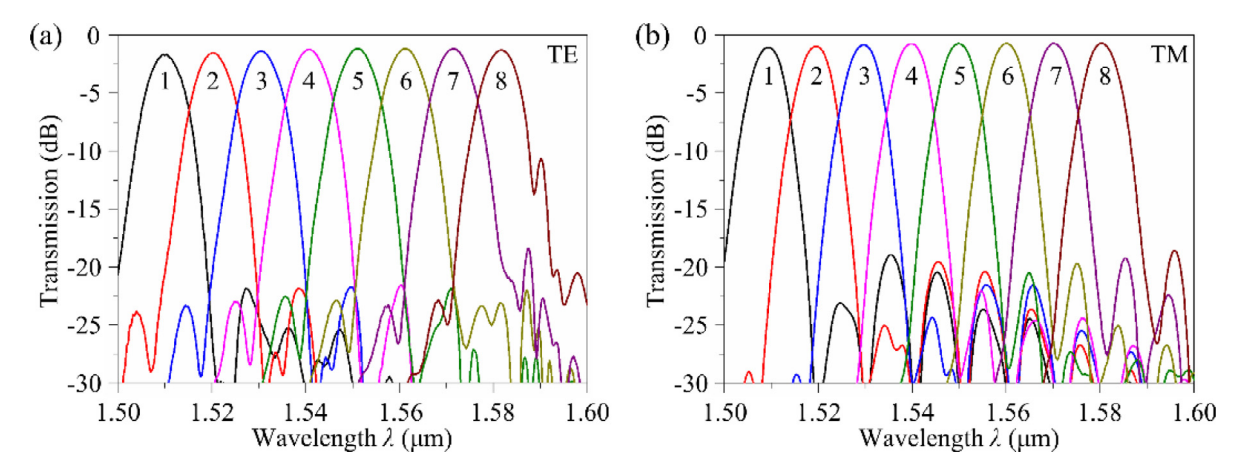


Fig. 10. Output spectra of the CDG with N=1 and  $\Delta\lambda=10$  nm for (a) TE ( $\varphi_1=6^\circ$ ) and (b) TM ( $\varphi_2=2^\circ$ ) modes.

Table 2
Comparison of simulation results between different diffraction grating designs on the SOI platform. PT=polarization; TK=SOI thickness; CN=channel number; CS=channel spacing; IL=insertion loss; NU=non-uniformity; CT=next-channel crosstalk; FT=footprint.

Reference	PT	TK	CN	CS	IL	NU	CT	FT
		(nm)		(nm)	(dB)	(dB)	(dB)	$(mm \times mm)$
[22]	TE	220	4	20	-0.7	0.9	/	$0.28 \times 0.15$
[18]	TE	220	13	3	-1.89	0.44	-52	$0.5 \times 0.8$
[23]	TE	220	9	16	-0.26	0.09	-22	/
[17]	TE	300	16	0.8	-1.45	0.5	-29	$2 \times 1.3$
This work	TE and TM	220	5 × 2	16	TE: -0.65 TM: -0.32	TE: 0.47 TM: 0.34	TE: -25 TM: -30	0.5 × 0.5
			8 × 2	10	TE: -1.30 TM: -0.70	TE: 0.58 TM: 0.35	TE: -20 TM: -23	0.8 × 0.6

individual channels diminish dramatically, especially for channel 5 of TE mode [18% (-7.41 dB)]. On the basis of the arguments presented, this deterioration is mostly due to the creation of many unwanted diffraction orders and the variation of the main order. Therefore, such a configuration is not optimal for broad spectrum multiplexing.

## 4. Fabrication tolerance

The structure can be defined with deep-ultraviolet lithography, which is then used as a mask for the one-step 220-nm deep etch with an inductively coupled plasma etching process. In actual processing, many parameters may deviate from the ideal situation. The impact of various fabrication errors is discussed here.

## 4.1. Etching width

The minimum etching size in the device  $d_{\rm etc}=0.24~\mu{\rm m}$ , which is easy to implement in fabrication process. However, for practical reasons, there may be slight deviations in  $d_{\rm etc}$ . According to Eqs. (1) and (5), with the Bragg period d constant, the deviation of  $d_{\rm etc}$  is irrelevant to the diffraction performances as long as the band gap of Bragg reflectors is wide enough. Fig. 14 presents the simulated reflection spectra with different  $d_{\rm etc}$  for TE and TM polarizations. When  $d_{\rm etc}$  varies from 0.216  $\mu{\rm m}$  to 0.264  $\mu{\rm m}$  (corresponding to the deviation of  $d_{\rm etc}$  from –10% to 10%), the reflection bands of TE and TM polarizations are blue shifted by about 38 nm and 20 nm, respectively. But all gratings still allow efficient reflection for dual polarizations with efficiencies over 96% at the desired waveband 1.5–1.6  $\mu{\rm m}$ . Furthermore, take TE-mode as an example, the simulated efficiency diffracted into the design

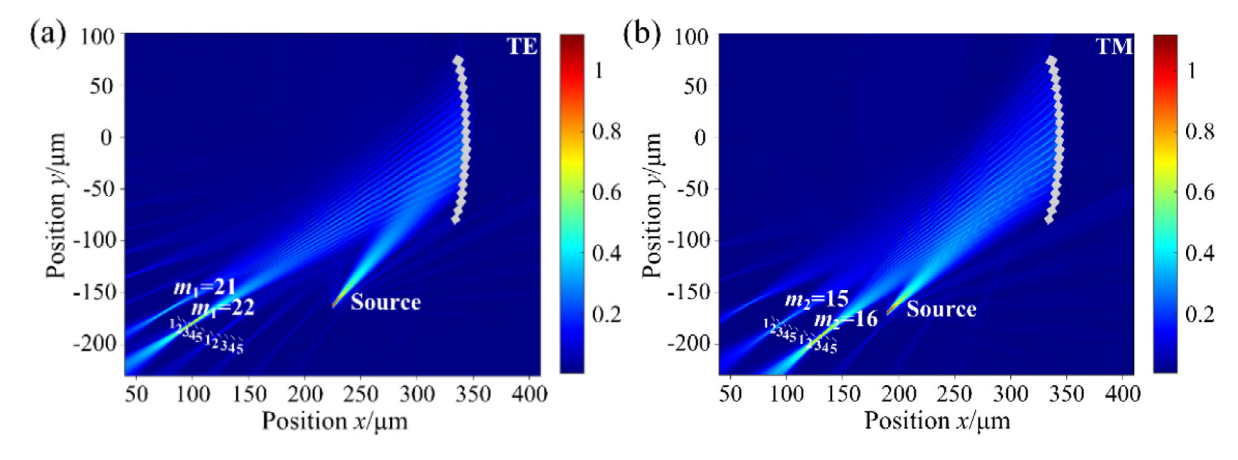


Fig. 11. Spatial distributions of lights in the CDG with a step configuration: 5 Bragg periods per grating period (N = 5) for (a) TE and (b) TM modes at the central wavelength.

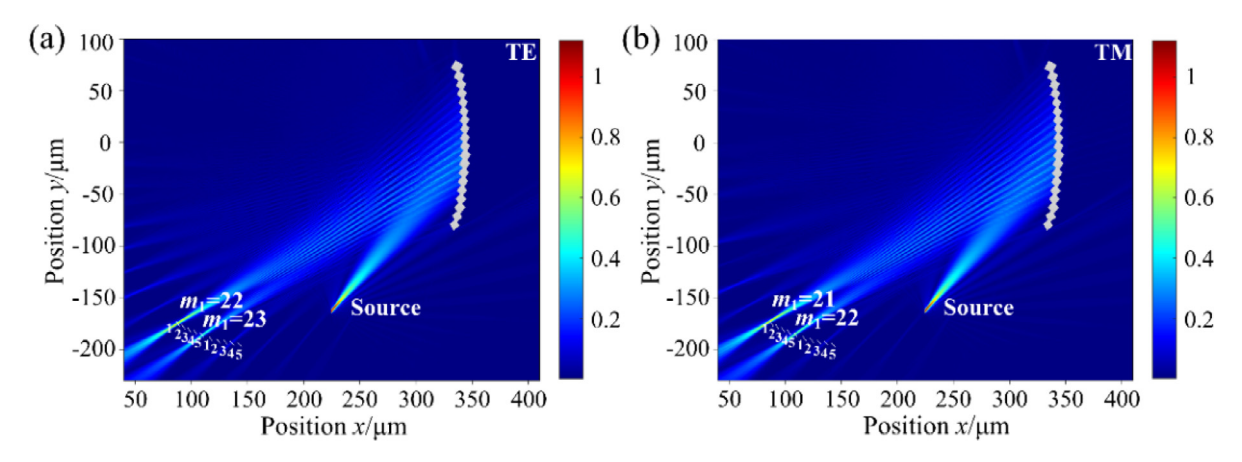


Fig. 12. Spatial distributions of lights with N=5 for TE mode at wavelengths of (a) 1.518  $\mu m$  and (b) 1.582  $\mu m$ .

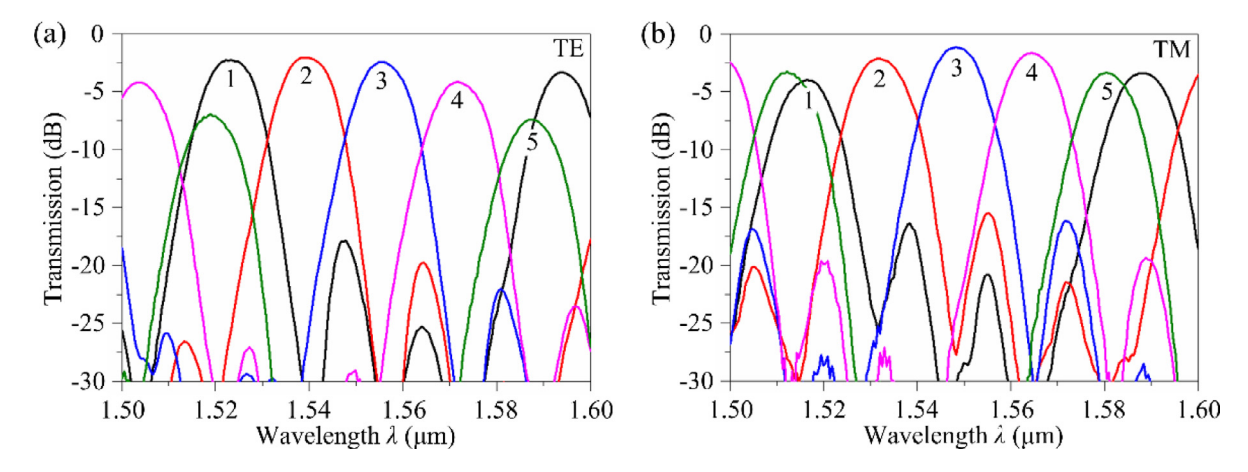


Fig. 13. Output spectra of the CDG with N=5 for (a) TE ( $\varphi_1=9^\circ$ ) and (b) TM ( $\varphi_2=3^\circ$ ) modes. (For interpretation of the references to color in this figure legend, the reader is referred to the web version of this article.)

order at  $\lambda_c$  changes less than 0.18 dB as  $d_{\rm etc}$  varies from 0.216  $\mu m$  to 0.264  $\mu m$ . Therefore, the designed CDG is very tolerant on fabrication imperfections of the etching width. A 10% trench width deviation does not lead to a significant decrease in grating efficiency.

## 4.2. Silicon thickness

The actual silicon thickness may differ from the design value, leading to the change of effective index of planar waveguide  $n_i$ . For the alternating strips and the slab region, the value of effective index

mainly affects reflection and diffraction performances, respectively. Fig. 15(a) shows the calculated values of  $n_i$  for the first four supported slab modes at  $\lambda_c$  under room temperature. The number of supported modes increases with increasing silicon thickness. The change of  $n_i$  will induce reflection waveband shift of the Bragg reflector, as presented in Fig. 15(b). For TM-mode, the reflector still provides high reflectivity over the band of 1.5–1.6  $\mu$ m as  $n_2$  varies from 2.04 to 2.08 (corresponding variation of silicon thickness is about  $\pm 3$  nm). While for TE-mode, due to the wider reflection band, the reflector is more robust to fabrication errors. The variation range of  $n_1$  is from 2.81 to

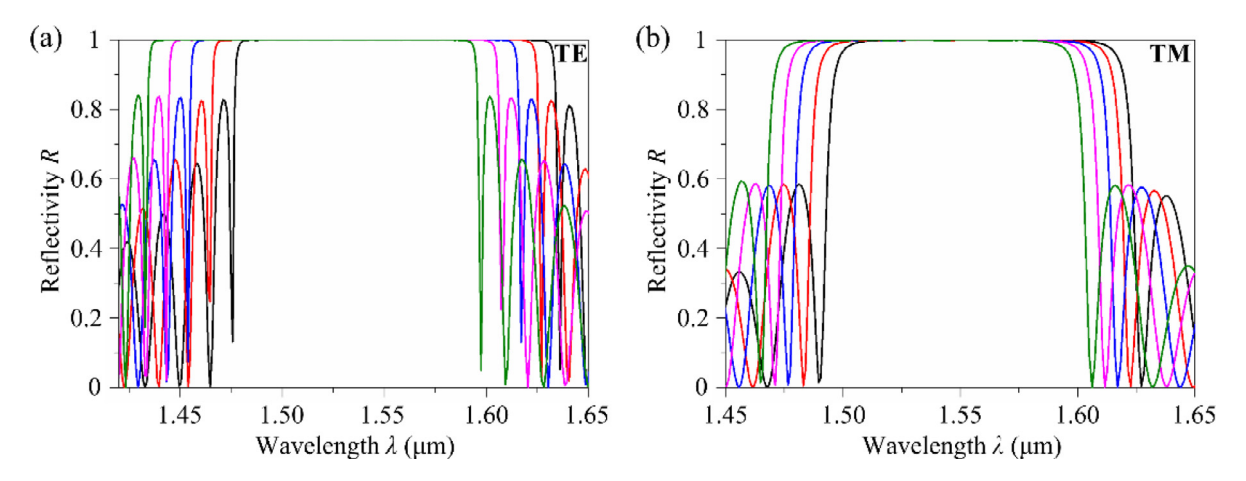


Fig. 14. Reflection spectra of the Bragg reflector for (a) TE and (b) TM modes with  $d_{\rm etc}$  from 0.216  $\mu$ m to 0.264  $\mu$ m.  $d_{\rm etc}=0.216$   $\mu$ m, black;  $d_{\rm etc}=0.228$   $\mu$ m, region (For interpretation of the references to color in this figure legend, the reader is referred to the web version of this article.)

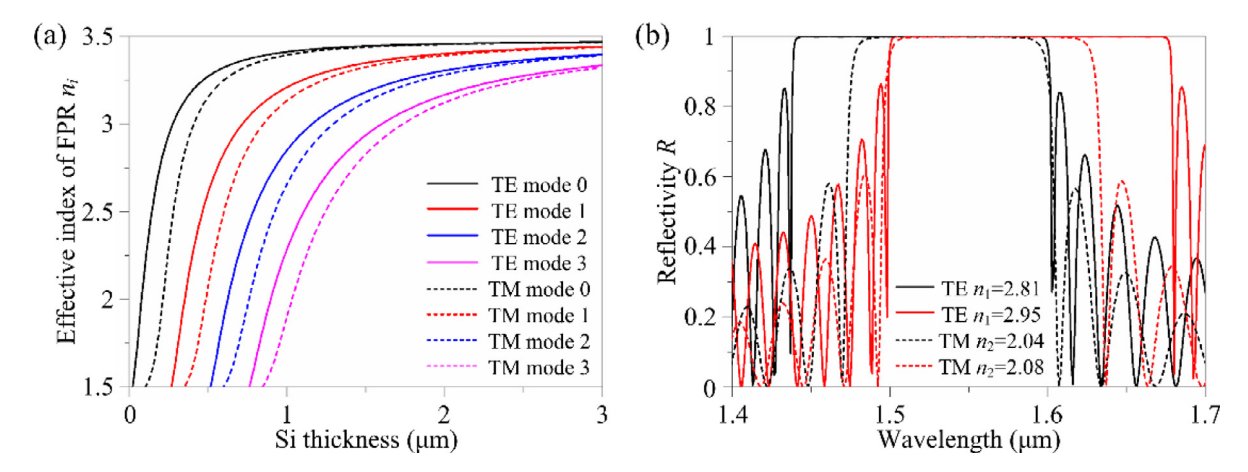


Fig. 15. (a) Effective index  $n_i$  at  $\lambda_c$  under various Si thickness; (b) Reflection spectra of the Bragg reflector with different  $n_i$  ( $\varphi_1$ =6°,  $\varphi_2$ =2°).

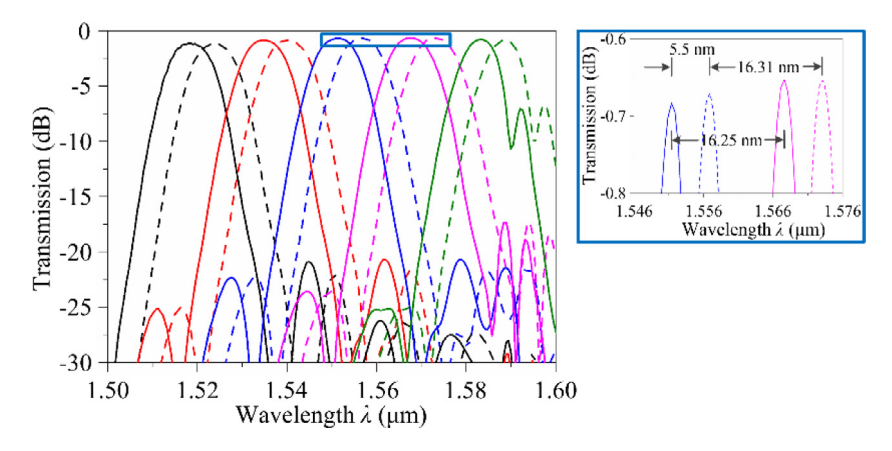


Fig. 16. Comparison of the output spectra for TE-mode with Si thickness of 220 nm (solid) and 223 nm (dash).

2.95, meaning the allowable thickness variation of about  $\pm 23$  nm. On the other hand, silicon thickness variation will also affect diffraction performances of the grating, which is mainly manifested as the shift of the diffraction spectrum. According to Eq. (2), we have

$$\frac{\Delta \lambda'}{\Delta \lambda} = \frac{n_i'}{n_i},\tag{13}$$

$$\lambda_{\text{shift}} = \frac{\left| n_i' - n_i \right|}{n_i} \lambda. \tag{14}$$

 $\Delta\lambda'$  is the channel spacing with effective index  $n_i'$ . The channel wavelength shift  $\lambda_{\rm shift}$  is proportional to the effective index deviation. As an example, the output spectra for TE polarized light with a 223 nm silicon layer ( $n_1'=2.858$ ) is simulated and demonstrated in Fig. 16. Other parameters are the same as those in Fig. 9(a). Compared with the situation of 220-nm-thick SOI, the channel spacing increases slightly by about 60 pm, and the diffraction spectrum is red shifted by about 5.5 nm with stable peak efficiency and crosstalk level. Therefore, when designing such demultiplexer device, effective index change induced by silicon thickness variation should be taken into account seriously.

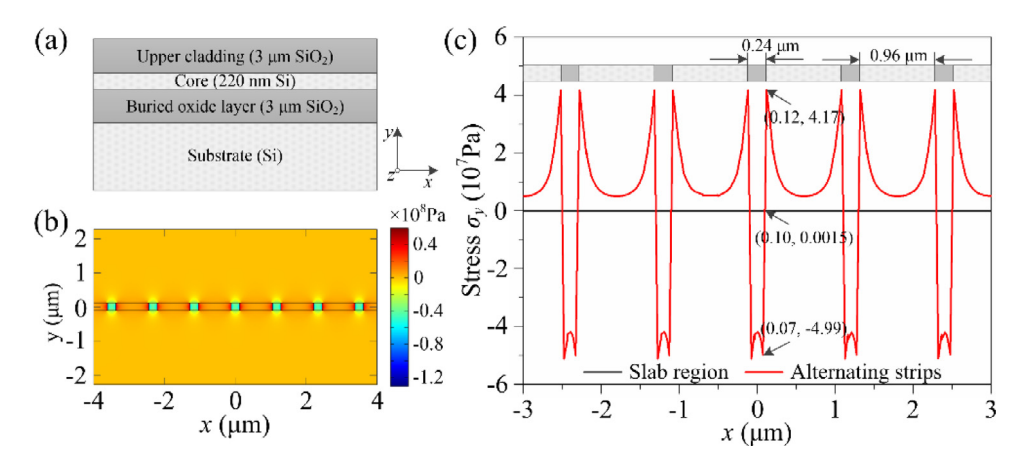


**Fig. 17.** (a) Cross section of the planar waveguide; (b) Stress distributions in y direction  $\sigma_y$ ; (c)  $\sigma_y$  on the centerline of the silicon core (slab region, black; alternating strips, red). (For interpretation of the references to color in this figure legend, the reader is referred to the web version of this article.)

## 4.3. Stress effects

In the previous analysis, the dielectric is assumed to be at stress free state. While due to fabrication and packaging, stresses are unavoidable in this multi-layer structure with diverse materials, which can change the distribution of refractive index. Note that the silicon layer in this case is covered by a silica cladding layer, which is usually fabricated by plasma enhanced chemical vapor deposition at high temperature of about 300 °C and then cooled down to room temperature. Fig. 17(a) shows the cross section of the planar waveguide. Due to the thermal mismatch of different layers, residual stresses are induced in both the slab region and the alternating strips. Fig. 17(b) presents stress distributions in y direction ( $\sigma_v$ ) at the cross section of the alternating strips, simulated by the finite element method of COMSOL software. The stress on the centerline of etched alternating strips (on the order of 10<sup>7</sup> Pa) is significantly stronger than that of the slab region (on the order of 10<sup>4</sup> Pa), as shown in Fig. 17(c). To study the stress magnitude effect, the index is assumed to be isotropic and homogeneous. According to the photo-elastic effect, with stress-optic constants on the order of 10<sup>-11</sup> Pa<sup>-1</sup> [24], the refractive index change caused by these stresses is between  $\pm 10^{-3}$  for the strips and  $\pm 10^{-6}$  for the slab region, which has little effect on the spectral response for both TE and TM polarizations based on the above analysis.

## 4.4. Temperature effects

The refractive index of material varies with operating temperature, which is known as thermos-optic effect. At room temperature, the thermo-optic coefficient of silicon and silica at  $\lambda_c$  is about  $1.8\times10^{-4}$  K<sup>-1</sup> and  $8.5\times10^{-6}$  K<sup>-1</sup>, respectively [25]. Therefore, silicon plays a major role in the thermo-optic effect of this device. With stable spectral response in terms of reflection waveband, channel spacing, peak efficiency and also crosstalk level, the thermal shift of channel wavelength is determined to be below 0.10 nm/°C and 0.14 nm/°C for TE and TM polarizations, respectively. Athermal design can be implemented to further reduce the need for active temperature stabilization and consequently the energy required to operate the device [26].

## 5. Conclusion

We demonstrate a novel Bragg-CDG for WDM-PDM applications on 220 nm SOI platform, which increase the utilization of incident light and provides a potential solution to enhance the link capacity greatly. Using the band gaps calculated by 1D PC bandgap theory, polarization-independent Bragg reflector is realized with a broad bandwidth (>100 nm), and is thus very robust to fabrication variations. TE and TM polarized light are incident into the same grating at different

angles and then refocused on separate locations. The dual incident angles are designed according to three necessary conditions. As an example, the designed CDG has 16 channels (8 wavelengths and dual polarizations) and 10 nm channel spacing with a very small footprint of  $0.8\times0.6~\text{mm}^2$ . The simulated on-chip loss is -1.30~dB and -0.70~dB for TE and TM polarizations, respectively. The step teeth configuration leads to a device degradation induced by the free spectral range limitation and the presence of multiple diffraction orders. Furthermore, the CDG is very tolerant on fabrication imperfections of etching width and stress effects during deposition process. But the variation of effective index of planar waveguide induced by the silicon thickness deviation can cause a considerable spectral shift, which should be strictly controlled in the fabrication.

## **Declaration of competing interest**

The authors declare that they have no known competing financial interests or personal relationships that could have appeared to influence the work reported in this paper.

#### Acknowledgments

This work was supported by the National Natural Science Foundation of China (Grant No. 61890961) and the Natural Science Basic Research Plan in Shaanxi Province of China (Grant No. 2018JM6008). The authors acknowledge X. She and J. Yao for valuable help in the stress effects analysis.

## References

- R.W. Tkach, Scaling optical communications for the next decade and beyond, Bell Labs Tech. J. 14 (2010) 3–9.
- [2] D. Dai, Silicon nanophotonic integrated devices for on-chip multiplexing and switching, J. Lightwave Technol. 35 (2017) 572–587.
- [3] H. Xu, L. Liu, Y. Shi, Polarization-insensitive four-channel coarse wavelength-division (de)multiplexer based on mach-zehnder interferometers with bent directional couplers and polarization rotators, Opt. Lett. 43 (2018) 1483-1486.
- [4] G. Jiang, S. Baig, H. Lu, K. Shen, M.R. Wang, Planar concave grating wavelength demultiplexers with flattened spectral response based on SU-8 polymer waveguides, Opt. Eng. 55 (2016) 037104.
- [5] C. Sciancalepore, R.J. Lycett, J.A. Dallery, S. Pauliac, K. Hassan, J. Harduin, H. Duprez, U. Weidenmueller, D.F.G. Gallagher, S. Menezo, B.B. Bakir, Low-crosstalk fabrication-insensitive echelle grating demultiplexers on silicon-on-insulator, IEEE Photonics Technol. Lett. 27 (2015) 494–497.
- [6] Z. Zhou, B. Bai, L. Liu, Silicon on-chip PDM and WDM technologies via plasmonics and subwavelength grating, IEEE J. Sel. Top. Quantum Electron. 25 (2019) 1–13.
- [7] W. Jin, K.S. Chiang, Three-dimensional long-period waveguide gratings for mode-division-multiplexing applications, Opt Express 26 (2018) 15289–15299.

- [8] O.M. Nawwar, H.M.H. Shalaby, R.K. Pokharel, Modeling, simulation and fabrication of bi-directional mode-division multiplexing for silicon-on-insulator platform, Appl. Opt. 57 (2018) 42–51.
- [9] Z. Xu, Q. Jin, Z. Tu, S. Gao, All-optical wavelength conversion for telecommunication mode-division multiplexing signals in integrated silicon waveguides, Appl. Opt. 57 (2018) 5036–5042.
- [10] S. Pathak, P. Dumon, D. Van Thourhout, W. Bogaerts, Comparison of AWGs and Echelle gratings for wavelength division multiplexing on silicon-on-insulator, IEEE Photonics J. 6 (2014) 1–9.
- [11] Y. Mao, J. Zhu, K. Li, B. Du, X. Hou, Perfect matching of concave diffraction grating with continuously circular Bragg mirrors on SOI platform, J. Opt. Soc. Amer. A 36 (2019) 641–646.
- [12] J. Brouckaert, W. Bogaerts, S. Selvaraja, P. Dumon, R. Baets, D. Van Thourhout, Planar concave grating demultiplexer with high reflective bragg reflector facets, IEEE Photonics Technol. Lett. 20 (2008) 309–311.
- [13] B. Du, J. Zhu, Y. Mao, B. Li, Y. Zhang, X. Hou, A design method based on photonic crystal theory for bragg concave diffraction grating, Opt. Commun. 385 (2017) 92–96.
- [14] Y. Mao, J. Zhu, K. Li, Y. Zhang, X. Hou, Dual-input concave diffraction grating demultiplexer based on dielectric multidirectional reflectors, J. Opt. Soc. Amer. A 36 (2019) 1585–1590.
- [15] S. Janz, A. Balakrishnan, S. Charbonneau, P. Cheben, M. Cloutier, A. Delage, K. Dossou, L. Erickson, M. Gao, P.A. Krug, B. Lamontagne, M. Packirisamy, M. Pearson, D.X. Xu, Planar waveguide echelle gratings in silica-on-silicon, IEEE Photonics Technol. Lett. 16 (2004) 503–505.
- [16] J. Pello, M. Muneeb, S. Keyvaninia, J.J.G.M. van der Tol, G. Roelkens, M.K. Smit, Planar concave grating demultiplexers on an inp-membrane-on-silicon photonic platform, IEEE Photonics Technol. Lett. 25 (2013) 1969–1972.

- [17] X. Pommarede, K. Hassan, P. Billondeau, V. Hugues, P. Grosse, B. Charbonnier, G.H. Duan, 16×100 GHz Echelle grating-based wavelength multiplexer on silicon-on-insulator platform, IEEE Photonics Technol. Lett. 29 (2017) 493–495.
- [18] R.J. Lycett, D.F.G. Gallagher, V.J. Brulis, Perfect chirped Echelle grating wavelength multiplexor: Design and optimization, IEEE Photonics J. 5 (2013) 2400123.
- [19] J.-J. He, E.S. Koteles, B. Lamontagne, L. Erickson, A. Delâge, M. Davies, Integrated polarization compensator for WDM waveguide demultiplexers, IEEE Photonics Technol. Lett. 11 (1999) 224–226.
- [20] D. Feng, W. Qian, H. Liang, C.C. Kung, J. Fong, B.J. Luff, M. Asghari, Fabrication insensitive echelle grating in silicon on insulator platform, IEEE Photonics Technol. Lett. 23 (2011) 284–286.
- [21] H. Wu, Y. Tan, D. Dai, Ultra-broadband high-performance polarizing beam splitter on silicon, Opt. Express 25 (2017) 6069–6075.
- [22] J. Brouckaert, W. Bogaerts, P. Dumon, D. Van Thourhout, R. Baets, Planar concave grating demultiplexer fabricated on a nanophotonic silicon-on-insulator platform, J. Lightwave Technol. 25 (2007) 1269–1275.
- [23] P. Pottier, M.J. Strain, M. Packirisamy, Integrated microspectrometer with elliptical bragg mirror enhanced diffraction grating on silicon on insulator, ACS Photon. 1 (2014) 430–436.
- [24] M. Huang, Stress effects on the performance of optical waveguides, Int. J. Solids Struct. 40 (2003) 1615–1632.
- [25] J. Komma, C. Schwarz, G. Hofmann, D. Heinert, R. Nawrodt, Thermo-optic coefficient of silicon at 1550 nm and cryogenic temperatures, Appl. Phys. Lett. 101 (2012) 041905.
- [26] D. Melati, P.G. Verly, A. Delage, P. Cheben, J.H. Schmid, S. Janz, D.X. Xu, Athermal echelle grating filter in silicon-on-insulator using a temperature-synchronized input, Opt. Express 26 (2018) 28651–28660.